mathematics

MDPI

Article

Indirect Neural-Enhanced Integral Sliding Mode Control for Finite-Time Fault-Tolerant Attitude Tracking of Spacecraft

Qijia Yao [1], Hadi Jahanshahi [2,*], Stelios Bekiros [3,4,5], Sanda Florentina Mihalache [6] and Naif D. Alotaibi [7]

1 School of Aerospace Engineering, Beijing Institute of Technology, Beijing 100081, China; qijia_yao@126.com
2 Department of Mechanical Engineering, University of Manitoba, Winnipeg, MB R3T 5V6, Canada
3 FEMA, University of Malta, MSD 2080 Msida, Malta; stelios.bekiros@um.edu.mt or s.bekiros@lse.ac.uk or s.bekiros@ipag.fr
4 LSE Health, Department of Health Policy, London School of Economics and Political Science, London WC2A 2AE, UK
5 IPAG Business School (IPAG), 184 Boulevard Saint-Germain, 75006 Paris, France
6 Automatic Control, Computers & Electronics Department, Petroleum-Gas University of Ploiești, 100680 Ploiești, Romania; sfrancu@upg-ploiesti.ro
7 Department of Electrical and Computer Engineering, Faculty of Engineering, King Abdulaziz University, Jeddah 21589, Saudi Arabia; ndalotabi@kau.edu.sa
* Correspondence: jahanshahi.hadi90@gmail.com

Abstract: In this article, a neural integral sliding mode control strategy is presented for the finite-time fault-tolerant attitude tracking of rigid spacecraft subject to unknown inertia and disturbances. First, an integral sliding mode controller was developed by originally constructing a novel integral sliding mode surface to avoid the singularity problem. Then, the neural network (NN) was embedded into the integral sliding mode controller to compensate the lumped uncertainty and replace the robust switching term. In this way, the chattering phenomenon was significantly suppressed. Particularly, the mechanism of indirect neural approximation was introduced through inequality relaxation. Benefiting from this design, only a single learning parameter was required to be adjusted online, and the computation burden of the proposed controller was extremely reduced. The stability argument showed that the proposed controller could guarantee that the attitude and angular velocity tracking errors were regulated to the minor residual sets around zero in a finite time. It was noteworthy that the proposed controller was not only strongly robust against unknown inertia and disturbances, but also highly insensitive to actuator faults. Finally, the effectiveness and advantages of the proposed control strategy were validated using simulations and comparisons.

Keywords: attitude tracking control; finite-time control; fault-tolerant control; integral sliding mode control; indirect neural approximation

MSC: 37N35; 93C40; 93D15

Citation: Yao, Q.; Jahanshahi, H.; Bekiros, S.; Mihalache, S.F.; Alotaibi, N.D. Indirect Neural-Enhanced Integral Sliding Mode Control for Finite-Time Fault-Tolerant Attitude Tracking of Spacecraft. *Mathematics* **2022**, *10*, 2467. https://doi.org/10.3390/math10142467

Academic Editor: Asier Ibeas

Received: 31 May 2022
Accepted: 11 July 2022
Published: 15 July 2022

1. Introduction

Attitude control is the premise and foundation for spacecraft to fulfill various space missions, such as on-orbit servicing, space debris removal, and deep space exploration. To meet the autonomy and intelligence trends, modern spacecraft are expected to have the capability of producing rapid, exact, and reliable responses to different maneuvering signals. On the one hand, a spacecraft is unavoidably affected by inertia uncertainty and disturbances due to the complex space environment. Even worse, the inertia matrix of the spacecraft may be fully unknown in some extreme cases. For example, after a space manipulator grasps a non-cooperative target, the inertia matrix of the combined spacecraft during the attitude takeover phase may be fully unknown. On the other hand, a spacecraft frequently suffers from actuator faults during practical applications. Until recently, a large number of control methods have been utilized in the design of spacecraft attitude control

systems, including proportional–differential (PD) control [1–4], sliding mode control [5–8], backstepping control [9,10], iterative learning control [11,12], and intelligent control [13–16].

The convergence property is an important performance index for the attitude control of spacecraft. Nevertheless, the above controllers can only realize the asymptotic stability or at best exponential stability of the closed-loop system. Alternatively, the finite-time control can guarantee that the attitude and angular velocity tracking errors are regulated to zero or the minor residual sets around zero in finite time. The finite-time control approaches for the attitude tracking of spacecraft can be roughly classified into three types. They are the homogeneous method [17–20], the technique of adding a power integrator [21–24], and the terminal sliding mode control [25–32]. It should be pointed out that the finite settling time of the homogeneous method is difficult to b estimate, and the technique of adding a power integrator is unable to handle the inertia uncertainty and disturbances. From the above analysis, the terminal sliding mode control was determined to be the best one among these three approaches to the design of spacecraft attitude control systems.

Nevertheless, the terminal sliding mode control exhibits two main disadvantages. The first disadvantage is the singularity problem, in which infinite control inputs are required to exactly steer the system states to zero. Although several types of nonsingular terminal sliding mode controllers have been developed, the singularity problem is avoided at the expense of losing part of the convergence rate. It should be emphasized that the full-order sliding mode controller in [33] and the integral sliding mode controller in [34] could realize the finite-time attitude tracking of spacecraft with no singularity problem. The sliding mode surfaces in these controllers were both designed based on the homogeneous method. The second disadvantage is the chattering phenomenon inherently existing in the sliding mode control. It is well recognized that neural networks (NNs) and fuzzy logic systems have a powerful universal approximation capability [35–44]. Since the chattering phenomenon is mainly caused by the robust switching term, an effective method for chattering suppression is adopting an NN or fuzzy logic system to replace the robust switching term. In [45], a finite-time attitude tracking control scheme for spacecraft was proposed by combining a terminal sliding mode control and a Chebyshev neural network. Moreover, in [46], a fuzzy nonsingular terminal sliding mode controller was designed for the finite-time attitude tracking of spacecraft subject to actuator faults. However, these controllers are difficult to be implemented in real time, since the conventional neural and fuzzy approximations require a large number of adaptive parameters to be learned online, and thus the spacecraft attitude control system inevitably suffers from a heavy computational burden. Consequently, the finite-time attitude tracking of spacecraft is still an open problem that deserves to be further addressed.

The above observations motivated our study. This article presents a neural integral sliding mode control strategy for the finite-time fault-tolerant attitude tracking of rigid spacecraft subject to unknown inertia and disturbances. The major novelties of this study can be summarized as the following three aspects.

- A novel integral sliding mode surface was constructed by utilizing the technique of adding a power integrator, based on which the integral sliding mode controller was developed with no singularity problem existing in the conventional terminal sliding mode control.
- The NN was embedded into the integral sliding mode controller to compensate the lumped uncertainty and replace the robust switching term. In this way, the chattering phenomenon was significantly suppressed. Particularly, the mechanism of indirect neural approximation was introduced through inequality relaxation. Benefiting from this design, only a single learning parameter was required to be adjusted online, and thus the proposed controller was computationally simple, which made it suitable for onboard implementations.
- The practical finite-time stability of the resulting closed-loop system was theoretically achieved. The proposed controller could guarantee that the attitude and angular velocity tracking errors were regulated to the minor residual sets around zero in a finite time.

It was noteworthy that the proposed controller was not only strongly robust against unknown inertia and disturbances, but also highly insensitive to actuator faults.

The rest of this paper is outlined as follows. Section 2 describes the problem and provides some preliminaries. Section 3 presents the control design and stability argument. Section 4 provides the simulations and comparisons. Lastly, Section 5 concludes this research.

2. Problem Description and Preliminaries

2.1. Notations

The following notations will be used in this article. $\mathbf{I}_n$ denotes the $n \times n$ identity matrix. $\|\cdot\|$ denotes the Euclidean norm of a vector or the induced norm of a matrix. $\lambda_{\min}(\cdot)$ and $\lambda_{\max}(\cdot)$ stand for the minimum and maximum eigenvalues of a matrix, respectively. For a vector $\boldsymbol{x} = [x_1, x_2, \ldots, x_n]^{\mathrm{T}}$ and a fraction power p, $\boldsymbol{x}^p = \left[x_1^p, x_2^p, \ldots, x_n^p\right]^{\mathrm{T}}$ and $\mathrm{sig}^p(\boldsymbol{x}) = \left[|x_1|^p \mathrm{sgn}(x_1), |x_2|^p \mathrm{sgn}(x_2), \ldots, |x_n|^p \mathrm{sgn}(x_n)\right]^{\mathrm{T}}$. $(\cdot)^{\times}$ denote the 3×3 skew-symmetric matrix of a vector. For a vector $\boldsymbol{a} = [a_1, a_2, a_3]^{\mathrm{T}}$, $\boldsymbol{a}^{\times}$ can be expressed as:

$$\boldsymbol{a}^{\times} = \begin{bmatrix} 0 & -a_3 & a_2 \\ a_3 & 0 & -a_1 \\ -a_2 & a_1 & 0 \end{bmatrix}. \tag{1}$$

2.2. Problem Statement

The spacecraft was modeled as a rigid body with no momentum transfer devices. The modified Rodrigues parameters (MRPs) were applied to represent the attitude motion of the spacecraft with respect to the inertial frame, denoted as $\boldsymbol{\sigma} = \boldsymbol{\rho} \tan\left(\frac{\theta}{4}\right) \in \mathbb{R}^3$, where $\boldsymbol{\rho}$ is the unit vector of the Euler axis and $\theta \in (-2\pi, 2\pi)$ is the rotation angle around the Euler axis. The attitude kinematics and dynamics of the spacecraft in the presence of actuator faults can be described as [47]:

$$\dot{\boldsymbol{\sigma}} = \boldsymbol{G}(\boldsymbol{\sigma})\boldsymbol{\omega}, \tag{2}$$

$$\boldsymbol{J}\dot{\boldsymbol{\omega}} = -\boldsymbol{\omega}^{\times}\boldsymbol{J}\boldsymbol{\omega} + \boldsymbol{\Gamma}\boldsymbol{u} + \boldsymbol{d}, \tag{3}$$

where $\boldsymbol{\omega} = [\omega_1, \omega_2, \omega_3]^{\mathrm{T}} \in \mathbb{R}^3$ denotes the angular velocity of the spacecraft with respect to the inertial frame and expressed in the body frame. $\boldsymbol{J} \in \mathbb{R}^{3\times3}$ is the inertia matrix of the spacecraft, which may be fully unknown in some extreme cases. $\boldsymbol{u} \in \mathbb{R}^3$ and $\boldsymbol{d} \in \mathbb{R}^3$ are the control torques and disturbances, respectively. $\boldsymbol{\Gamma} = \mathrm{diag}\{\gamma_1, \gamma_2, \gamma_3\}$ is the actuation effectiveness matrix with $0 \le \gamma_i \le 1$ $(i = 1, 2, 3)$. The cases $\gamma_i = 1$, $0 < \gamma_i < 1$, and $\gamma_i = 0$ represent whether the corresponding control torque is healthy, partially faulty, or completely failed, respectively. In this article, the spacecraft was supposed to be fully actuated with $0 < \gamma_i \le 1$ $(i = 1, 2, 3)$. $\boldsymbol{G}(\boldsymbol{\sigma}) \in \mathbb{R}^{3\times3}$ is the Jacobian matrix, denoted as:

$$\boldsymbol{G}(\boldsymbol{\sigma}) = \frac{1}{2}\left(\frac{1 - \boldsymbol{\sigma}^{\mathrm{T}}\boldsymbol{\sigma}}{2}\mathbf{I}_3 + \boldsymbol{\sigma}^{\times} + \boldsymbol{\sigma}\boldsymbol{\sigma}^{\mathrm{T}}\right). \tag{4}$$

$\boldsymbol{G}(\boldsymbol{\sigma})$ has the properties $\boldsymbol{\sigma}^{\mathrm{T}}\boldsymbol{G}(\boldsymbol{\sigma}) = \frac{1+\boldsymbol{\sigma}^{\mathrm{T}}\boldsymbol{\sigma}}{4}\boldsymbol{\sigma}^{\mathrm{T}}$ and $\|\boldsymbol{G}(\boldsymbol{\sigma})\| = \frac{1+\boldsymbol{\sigma}^{\mathrm{T}}\boldsymbol{\sigma}}{4}$.

Let $\boldsymbol{\sigma}_{\mathrm{d}}$ and $\boldsymbol{\omega}_{\mathrm{d}}$ be the desired attitude and angular velocity of the spacecraft, respectively. Then, the attitude and angular velocity tracking errors can be defined as:

$$\boldsymbol{\sigma}_e = \boldsymbol{\sigma} \otimes \boldsymbol{\sigma}_{\mathrm{d}}^{-1} = \frac{\left(1 - \boldsymbol{\sigma}_{\mathrm{d}}^{\mathrm{T}}\boldsymbol{\sigma}_{\mathrm{d}}\right)\boldsymbol{\sigma} - \left(1 - \boldsymbol{\sigma}^{\mathrm{T}}\boldsymbol{\sigma}\right)\boldsymbol{\sigma}_{\mathrm{d}} - 2\boldsymbol{S}(\boldsymbol{\sigma}_{\mathrm{d}})\boldsymbol{\sigma}}{1 + \boldsymbol{\sigma}_{\mathrm{d}}^{\mathrm{T}}\boldsymbol{\sigma}_{\mathrm{d}}\boldsymbol{\sigma}^{\mathrm{T}}\boldsymbol{\sigma} + 2\boldsymbol{\sigma}_{\mathrm{d}}^{\mathrm{T}}\boldsymbol{\sigma}}, \tag{5}$$

$$\boldsymbol{\omega}_e = \boldsymbol{\omega} - \boldsymbol{R}(\boldsymbol{\sigma}_e)\boldsymbol{\omega}_{\mathrm{d}}, \tag{6}$$

where $\boldsymbol{R}(\sigma_e) \in \mathbb{R}^{3\times3}$ is the rotation matrix from the desired frame to the body frame, denoted as:

$$\boldsymbol{R}(\sigma_e) = \mathbf{I}_3 + \frac{8\sigma_e^{\times}\sigma_e^{\times} - 4\left(1-\sigma_e^{\mathrm{T}}\sigma_e\right)\sigma_e^{\times}}{\left(1+\sigma_e^{\mathrm{T}}\sigma_e\right)^2}. \tag{7}$$

$\boldsymbol{R}(\sigma_e)$ has the property $\dot{\boldsymbol{R}}(\sigma_e) = -\boldsymbol{\omega}_e^{\times}\boldsymbol{R}(\sigma_e)$. Subsequently, the error attitude kinematics and dynamics of the spacecraft can be derived as:

$$\dot{\sigma}_e = \boldsymbol{G}(\sigma_e)\boldsymbol{\omega}_e, \tag{8}$$

$$\boldsymbol{J}\dot{\boldsymbol{\omega}}_e = -\boldsymbol{\omega}^{\times}\boldsymbol{J}\boldsymbol{\omega} + \boldsymbol{J}\left(\boldsymbol{\omega}_e^{\times}\boldsymbol{R}(\sigma_e)\boldsymbol{\omega}_e - \boldsymbol{R}(\sigma_e)\dot{\boldsymbol{\omega}}_{\mathrm{d}}\right) + \boldsymbol{\Gamma}\boldsymbol{u} + \boldsymbol{d}. \tag{9}$$

The aim of this research was to develop a fault-tolerant controller for a spacecraft to realize attitude tracking in a finite time even when subject to unknown inertia and disturbances.

2.3. Useful Lemmas

Consider a nonlinear system:

$$\dot{\boldsymbol{x}} = \boldsymbol{f}(\boldsymbol{x}),\ \ \boldsymbol{f}(\mathbf{0}) = \mathbf{0},\ \ \boldsymbol{x} \in \mathbb{R}^n, \tag{10}$$

where $\boldsymbol{f}(\cdot) : \mathbb{R}^n \to \mathbb{R}^n$ is a continuous vector field.

Lemma 1 ([48]). *Suppose system (10); if there exists a positive definite function $V(\boldsymbol{x}) : \mathbb{R}^n \to \mathbb{R}$ satisfying $\dot{V}(\boldsymbol{x}) + \kappa V^p(\boldsymbol{x}) \le 0$, where $\kappa > 0$ and $0 < p < 1$, then system (10) is globally finite-time stable and $V(\boldsymbol{x})$ can regulate to zero in finite time. Moreover, the finite settling time can be estimated as $T \le \frac{V^{1-p}(0)}{\kappa(1-p)}$.*

Lemma 2 ([49]). *Suppose system (10); if there exists a positive definite function $V(\boldsymbol{x}) : \mathbb{R}^n \to \mathbb{R}$ satisfying $\dot{V}(\boldsymbol{x}) + \kappa_1 V(\boldsymbol{x}) + \kappa_2 V^p(\boldsymbol{x}) \le \vartheta$, where $\kappa_1 > 0$, $\kappa_2 > 0$, $0 < p < 1$, and $\vartheta > 0$, then system (10) is practically finite-time stable and $V(\boldsymbol{x})$ can regulate to the following minor residual set around zero in a finite time:*

$$C = \left\{ V(\boldsymbol{x}) \middle| V(\boldsymbol{x}) \le \frac{\vartheta}{(1-\varsigma)\kappa_1} \right\}, \tag{11}$$

where $0 < \varsigma < 1$. Moreover, the finite settling time can be estimated as $T \le \frac{1}{\varsigma\kappa_1(1-p)} \ln \frac{\varsigma\kappa_1 V^{1-p}(0)+\kappa_2}{\kappa_2}$.

Lemma 3 ([50]). *For a nonlinear function $f(\boldsymbol{Z})$, $\boldsymbol{Z} \in \mathbb{R}^n$, it can be approximated by a radial basis function NN (RBFNN) as:*

$$f(\boldsymbol{Z}) = \boldsymbol{W}^{*\mathrm{T}}\boldsymbol{\Phi}(\boldsymbol{Z}) + \varepsilon(\boldsymbol{Z}), \tag{12}$$

where $\boldsymbol{W}^* \in \mathbb{R}^N$ is the ideal RBFNN weight, $\boldsymbol{\Phi}(\boldsymbol{Z}) = [\varphi_1(\boldsymbol{Z}), \varphi_2(\boldsymbol{Z}), \ldots, \varphi_N(\boldsymbol{Z})]^{\mathrm{T}} \in \mathbb{R}^N$ is the basis function vector, $\varepsilon(\boldsymbol{Z})$ is the approximation error with $|\varepsilon(\boldsymbol{Z})| \le \bar{\varepsilon}$, $\bar{\varepsilon} > 0$, and N is the number of neurons. Moreover, $\varphi_i(\boldsymbol{Z})$ is commonly chosen as the Gaussian function:

$$\varphi_i(\boldsymbol{Z}) = \exp\left(-\|\boldsymbol{Z} - \boldsymbol{c}_i\|^2 / w_i^2\right),\ \ i = 1, 2, \ldots, N, \tag{13}$$

where $\boldsymbol{c}_i = [c_{i1}, c_{i2}, \ldots, c_{in}]^{\mathrm{T}} \in \mathbb{R}^n$ and w_i are the center and width of the Gaussian function, respectively.

Lemma 4 ([51]). *For any x_1, x_2, and $0 < p = p_1/p_2 \le 1$, where p_1 and p_2 are positive odd integers, the following inequality holds:*

$$\left| x_1^p - x_2^p \right| \le 2^{1-p}|x_1 - x_2|^p. \tag{14}$$

Lemma 5 ([51]). *For any x_1, x_2, $p > 0$, $q > 0$, and $r > 0$, the following inequality holds:*

$$|x_1|^p|x_2|^q \leq \frac{p}{p+q}r|x_1|^{p+q} + \frac{q}{p+q}r^{-\frac{p}{q}}|x_2|^{p+q}. \tag{15}$$

Lemma 6 ([51]). *For any x_i, $i = 1, 2, \ldots, n$, and $0 < p < 1$, the following inequality holds:*

$$(|x_1| + |x_2| + \cdots + |x_n|)^p \leq |x_1|^p + |x_2|^p + \cdots + |x_n|^p. \tag{16}$$

3. Control Design and Stability Argument

In this section, the main results of this study are presented. First, an integral sliding mode surface was constructed by utilizing the technique of adding a power integrator. Then, based on the integral sliding mode surface, a neural integral sliding mode controller was developed by adopting the NN to compensate the lumped uncertainty. Finally, the practical finite-time stability of the resulting closed-loop system was theoretically achieved.

3.1. Integral Sliding Mode Surface Design

By utilizing the technique of adding a power integrator, the integral sliding mode surface is constructed as:

$$\boldsymbol{s} = \boldsymbol{\omega}_e + \int_0^t h_2\left(\frac{1+\boldsymbol{\sigma}_e^{\mathrm{T}}(\tau)\boldsymbol{\sigma}_e(\tau)}{4}\right)\left(\boldsymbol{\omega}_e^p(\tau) + h_1^p\boldsymbol{\sigma}_e(\tau)\right)^{\frac{2}{p}-1}\mathrm{d}\tau, \tag{17}$$

where $1 < p = p_1/p_2 < 2$, and p_1 and p_2 are positive odd integers. Moreover, the design parameters h_1 and h_2 should be selected to satisfy the following conditions:

$$h_1 \geq \frac{2^{1-\frac{1}{p}}p+3}{1+p} + 2^{-\frac{1+p}{2p}}\alpha, \tag{18}$$

$$h_2 \geq 2^{2-\frac{2}{p}}3\left(2-\frac{1}{p}\right)h_1^p + \frac{2^{1-\frac{1}{p}}}{(1+p)}\left(2-\frac{1}{p}\right)\left(2^{1-\frac{1}{p}}+3p\right)h_1^{p+1} + 2^{1-\frac{1}{p}}\left(2-\frac{1}{p}\right)^{\frac{p-1}{2p}}h_1^{\frac{p^2-1}{2p}}\alpha, \tag{19}$$

where $\alpha > 0$.

Remark 1. *Different from the terminal sliding mode surface [25–32] and the full-order sliding mode surface and the integral sliding mode surface designed based on the homogeneous method [33,34], the integral sliding mode surface (17) was originally constructed by utilizing the adding a power integrator technique. Based on the integral sliding mode surface, the integral sliding mode controller could be developed with no singularity problem existing in the conventional terminal sliding mode control.*

Theorem 1. *When the integral sliding mode surface $\boldsymbol{s}$ arrives at zero, the attitude and angular velocity tracking errors $\boldsymbol{\sigma}_e$ and $\boldsymbol{\omega}_e$ can regulate to zero in finite time.*

Proof. Define the variables $\boldsymbol{\omega}_e^* = -h_1\boldsymbol{\sigma}_e^{\frac{1}{p}}$ and $\boldsymbol{\zeta} = \boldsymbol{\omega}_e^p - \boldsymbol{\omega}_e^{*p}$. When the integral sliding mode surface arrives at zero, we have:

$$\begin{cases} \dot{\boldsymbol{\sigma}}_e = \boldsymbol{\omega}_e, \\ \dot{\boldsymbol{\omega}}_e = -h_2\left(\frac{1+\boldsymbol{\sigma}_e^{\mathrm{T}}\boldsymbol{\sigma}_e}{4}\right)\boldsymbol{\zeta}^{\frac{2}{p}-1}. \end{cases} \tag{20}$$

Introduce the following Lyapunov candidate function:

$$L = L_0(\boldsymbol{\sigma}_e) + \sum_{i=1}^{3} L_i(\zeta_i), \tag{21}$$

where

$$L_0(\boldsymbol{\sigma}_e) = \frac{1}{2}\boldsymbol{\sigma}_e^{\mathrm{T}}\boldsymbol{\sigma}_e, \tag{22}$$

$$L_i(\zeta_i) = \frac{1}{2^{1-\frac{1}{p}}\left(2-\frac{1}{p}\right)h_1^{1+p}}\int_{\omega_{ei}^*}^{\omega_{ei}}\left(\varpi^p - \omega_{ci}^p\right)^{2-\frac{1}{p}}\mathrm{d}\varpi. \tag{23}$$

Employing Lemmas 4 and 5, the time differentiation of L_0 can be evaluated as:

$$\begin{aligned}
\dot{L}_0 &= \boldsymbol{\sigma}_e^{\mathrm{T}}\boldsymbol{G}(\boldsymbol{\sigma}_e)\boldsymbol{\omega}_e \\
&= \left(\tfrac{1+\boldsymbol{\sigma}_e^{\mathrm{T}}\boldsymbol{\sigma}_e}{4}\right)\left(\boldsymbol{\sigma}_e^{\mathrm{T}}\boldsymbol{\omega}_e + \boldsymbol{\sigma}_e^{\mathrm{T}}(\boldsymbol{\omega}_e - \boldsymbol{\omega}_e^*)\right) \\
&= \left(\tfrac{1+\boldsymbol{\sigma}_e^{\mathrm{T}}\boldsymbol{\sigma}_e}{4}\right)\left(-h_1\sum_{i=1}^{3}{\sigma_{ei}}^{1+\frac{1}{p}} + \boldsymbol{\sigma}_e^{\mathrm{T}}(\boldsymbol{\omega}_e - \boldsymbol{\omega}_e^*)\right) \\
&\le \left(\tfrac{1+\boldsymbol{\sigma}_e^{\mathrm{T}}\boldsymbol{\sigma}_e}{4}\right)\left(-h_1\sum_{i=1}^{3}|\sigma_{ei}|^{1+\frac{1}{p}} + 2^{1-\frac{1}{p}}\sum_{i=1}^{3}|\sigma_{ei}|\cdot|\zeta_i|^{\frac{1}{p}}\right) \\
&\le \left(\tfrac{1+\boldsymbol{\sigma}_e^{\mathrm{T}}\boldsymbol{\sigma}_e}{4}\right)\left(-\left(h_1 - \tfrac{2^{1-\frac{1}{p}}p}{1+p}\right)\sum_{i=1}^{3}|\sigma_{ei}|^{1+\frac{1}{p}} + \tfrac{2^{1-\frac{1}{p}}}{1+p}\sum_{i=1}^{3}|\zeta_i|^{1+\frac{1}{p}}\right).
\end{aligned} \tag{24}$$

Moreover, the time differentiation of L_i can be evaluated as:

$$\dot{L}_i = \frac{\mathrm{d}\omega_{ei}^{*p}/\mathrm{d}t}{2^{1-\frac{1}{p}}h_1^{1+p}}\int_{\omega_{ei}^*}^{\omega_{ei}}\left(\varpi^p - \omega_{ei}^{*p}\right)^{1-\frac{1}{p}}\mathrm{d}\varpi + \frac{\zeta_i^{2-\frac{1}{p}}\dot{\omega}_{ei}}{2^{1-\frac{1}{p}}\left(2-\frac{1}{p}\right)h_1^{1+p}}. \tag{25}$$

The following inequality can be easily derived:

$$\dot{L}_i = \frac{\mathrm{d}\omega_{ei}^{*p}/\mathrm{d}t}{2^{1-\frac{1}{p}}h_1^{1+p}}\int_{\omega_{ei}^*}^{\omega_{ei}}\left(\varpi^p - \omega_{ei}^{*p}\right)^{1-\frac{1}{p}}\mathrm{d}\varpi + \frac{\zeta_i^{2-\frac{1}{p}}\dot{\omega}_{ei}}{2^{1-\frac{1}{p}}\left(2-\frac{1}{p}\right)h_1^{1+p}}. \tag{26}$$

Substituting (26) into (25) and employing Lemma 4, we have:

$$\dot{L}_i \le \frac{1}{2^{1-\frac{1}{p}}h_1}\left(\frac{1+\boldsymbol{\sigma}_e^{\mathrm{T}}\boldsymbol{\sigma}_e}{4}\right)\left(\sum_{j=1}^{3}|\omega_{ej}|\right)|\omega_{ei} - \omega_{ei}^*||\zeta_i|^{1-\frac{1}{p}} + \frac{\zeta_i^{2-\frac{1}{p}}\dot{\omega}_{ei}}{2^{1-\frac{1}{p}}\left(2-\frac{1}{p}\right)h_1^{1+p}}. \tag{27}$$

Moreover, employing Lemmas 4 and 5, we have:

$$\begin{aligned}
\tfrac{1}{2^{1-\frac{1}{p}}h_1}\left|\omega_{ej}\right||\omega_{ei} - \omega_{ei}^*||\zeta_i|^{1-\frac{1}{p}} &\le \tfrac{1}{h_1}\left|\omega_{ej}\right||\zeta_i| \\
&\le \tfrac{1}{h_1}|\zeta_i|\left|\omega_{ej} - \omega_{ej}^*\right| + \tfrac{1}{h_1}|\zeta_i|\left|\omega_{ej}^*\right| \\
&\le \tfrac{p\left(2^{1-\frac{1}{p}}+h_1\right)}{(1+p)h_1}|\zeta_i|^{1+\frac{1}{p}} + \tfrac{2^{1-\frac{1}{p}}}{(1+p)h_1}\left|\zeta_j\right|^{1+\frac{1}{p}} + \tfrac{1}{1+p}\left|\sigma_{ej}\right|^{1+\frac{1}{p}}.
\end{aligned} \tag{28}$$

Substituting (28) into (27), we have:

$$\begin{aligned}\dot{L}_i \leq & \left(\frac{1+\sigma_e^{\mathrm{T}}\sigma_e}{4}\right)\left(\frac{3p\left(2^{1-\frac{1}{p}}+h_1\right)}{(1+p)h_1}|\zeta_i|^{1+\frac{1}{p}}+\frac{2^{1-\frac{1}{p}}}{(1+p)h_1}\sum_{j=1}^{3}|\zeta_j|^{1+\frac{1}{p}}+\frac{1}{1+p}\sum_{j=1}^{3}|\sigma_{ej}|^{1+\frac{1}{p}}\right)\\ &+\frac{\zeta_i^{2-\frac{1}{p}}\dot{\omega}_{ei}}{2^{1-\frac{1}{p}}\left(2-\frac{1}{p}\right)h_1^{1+p}}.\end{aligned} \tag{29}$$

Invoking (24) and (29), the time differentiation of L can be evaluated as:

$$\begin{aligned}\dot{L} &= \dot{L}_0+\sum_{i=1}^{3}\dot{L}_i\\ &\leq \left(\frac{1+\sigma_e^{\mathrm{T}}\sigma_e}{4}\right)\left(-\left(h_1-\frac{2^{1-\frac{1}{p}}p+3}{1+p}\right)\sum_{i=1}^{3}|\sigma_{ei}|^{1+\frac{1}{p}}+\left(\frac{2^{1-\frac{1}{p}}+3p}{1+p}+\frac{3\left(2^{1-\frac{1}{p}}\right)}{h_1}\right)\sum_{i=1}^{3}|\zeta_i|^{1+\frac{1}{p}}\right)\\ &\quad+\frac{\sum_{i=1}^{3}\zeta_i^{2-\frac{1}{p}}\dot{\omega}_{ei}}{2^{1-\frac{1}{p}}\left(2-\frac{1}{p}\right)h_1^{1+p}}.\end{aligned} \tag{30}$$

Substituting (20) into (30), we have:

$$\begin{aligned}\dot{L} \leq & \left(\frac{1+\sigma_e^{\mathrm{T}}\sigma_e}{4}\right)\left(-\left(h_1-\frac{2^{1-\frac{1}{p}}p+3}{1+p}\right)\sum_{i=1}^{3}|\sigma_{ei}|^{1+\frac{1}{p}}\right.\\ &\left.+\left(-\frac{2^{1-\frac{1}{p}}+3p}{1+p}-\frac{3\left(2^{1-\frac{1}{p}}\right)}{h_1}+\frac{h_2}{2^{1-\frac{1}{p}}\left(2-\frac{1}{p}\right)h_1^{1+p}}\right)\sum_{i=1}^{3}|\zeta_i|^{1+\frac{1}{p}}\right).\end{aligned} \tag{31}$$

On the other hand, employing Lemma 4 in (23), we have:

$$\begin{aligned}L_i &\leq \frac{1}{2^{1-\frac{1}{p}}\left(2-\frac{1}{p}\right)h_1^{1+p}}\left|\omega_{ei}-\omega_{ei}^*\right|\cdot|\zeta_i|^{2-\frac{1}{p}}\\ &\leq \frac{1}{\left(2-\frac{1}{p}\right)h_1^{1+p}}\zeta_i^2.\end{aligned} \tag{32}$$

Substituting (32) into (21) and employing Lemma 6, we have:

$$L^{\frac{1+p}{2p}} \leq \frac{1}{2^{\frac{1+p}{2p}}}\sum_{i=1}^{3}|\sigma_{ei}|^{1+\frac{1}{p}}+\frac{1}{\left(2-\frac{1}{p}\right)^{\frac{1+p}{2p}}h_1^{\frac{(1+p)^2}{2p}}}\sum_{i=1}^{3}|\zeta_i|^{1+\frac{1}{p}}. \tag{33}$$

Invoking (31) and (33), when the conditions (18) and (19) are satisfied, we further have:

$$\dot{L}+\alpha L^{\frac{1+p}{2p}} \leq 0. \tag{34}$$

Then, using Lemma 1, the closed-loop system (20) becomes globally finite-time stable. When the integral sliding mode surface $\boldsymbol{s}$ arrives at zero, the attitude and angular velocity tracking errors $\boldsymbol{\sigma}_e$ and $\boldsymbol{\omega}_e$ can regulate to zero in finite time. Moreover, the finite settling time of the sliding phase can be estimated as:

$$T_{sliding} \leq \frac{2pL^{\frac{p-1}{2p}}(0)}{\alpha(p-1)}. \tag{35}$$

The proof is thus finished. □

3.2. Neural Integral Sliding Mode Control Design

The time differentiation of $\boldsymbol{s}$ can be evaluated as:

$$\begin{aligned}\boldsymbol{J}\dot{\boldsymbol{s}} &= \boldsymbol{J}\dot{\boldsymbol{\omega}}_e + h_2\left(\tfrac{1+\boldsymbol{\sigma}_e^{\mathrm{T}}\boldsymbol{\sigma}_e}{4}\right)\boldsymbol{J}\left(\boldsymbol{\omega}_e^{p} + h_1^{p}\boldsymbol{\sigma}_e\right)^{\frac{2}{p}-1} \\ &= -\boldsymbol{\omega}^{\times}\boldsymbol{J}\boldsymbol{\omega} + \boldsymbol{J}\left(\boldsymbol{\omega}_e^{\times}\boldsymbol{R}(\boldsymbol{\sigma}_e)\boldsymbol{\omega}_e - \boldsymbol{R}(\boldsymbol{\sigma}_e)\dot{\boldsymbol{\omega}}_{\mathrm{d}}\right) + \boldsymbol{\Gamma}\boldsymbol{u} + \boldsymbol{d} \\ &\quad + h_2\left(\tfrac{1+\boldsymbol{\sigma}_e^{\mathrm{T}}\boldsymbol{\sigma}_e}{4}\right)\boldsymbol{J}\left(\boldsymbol{\omega}_e^{p} + h_1^{p}\boldsymbol{\sigma}_e\right)^{\frac{2}{p}-1} \\ &= \boldsymbol{\Gamma}\boldsymbol{u} + \boldsymbol{F},\end{aligned} \tag{36}$$

where $\boldsymbol{F}$ is the lumped uncertainty, denoted as:

$$\boldsymbol{F} = -\boldsymbol{\omega}^{\times}\boldsymbol{J}\boldsymbol{\omega} + \boldsymbol{J}\left(\boldsymbol{\omega}_e^{\times}\boldsymbol{R}(\boldsymbol{\sigma}_e)\boldsymbol{\omega}_e - \boldsymbol{R}(\boldsymbol{\sigma}_e)\dot{\boldsymbol{\omega}}_{\mathrm{d}}\right) + \boldsymbol{d} + h_2\left(\frac{1+\boldsymbol{\sigma}_e^{\mathrm{T}}\boldsymbol{\sigma}_e}{4}\right)\boldsymbol{J}\left(\boldsymbol{\omega}_e^{p} + h_1^{p}\boldsymbol{\sigma}_e\right)^{\frac{2}{p}-1}. \tag{37}$$

Define the variable $\boldsymbol{Z} = \left[\boldsymbol{\sigma}^{\mathrm{T}}, \boldsymbol{\omega}^{\mathrm{T}}\right]^{\mathrm{T}}$. According to Lemma 3, the lumped uncertainty can be expressed as:

$$\boldsymbol{F} = \boldsymbol{W}^{*\mathrm{T}}\boldsymbol{\Phi}(\boldsymbol{Z}) + \boldsymbol{\varepsilon}(\boldsymbol{Z}), \tag{38}$$

where $\boldsymbol{W}^{*} \in \mathbb{R}^{N\times 3}$ is the ideal RBFNN weight, $\boldsymbol{\Phi}(\boldsymbol{Z}) \in \mathbb{R}^{N}$ is the Gaussian basis function vector, $\boldsymbol{\varepsilon}(\boldsymbol{Z}) \in \mathbb{R}^{3}$ is the approximation error with $\|\boldsymbol{\varepsilon}(\boldsymbol{Z})\| \le \bar{\varepsilon}$, $\bar{\varepsilon} > 0$, and N is the number of neurons. Substituting $\|\boldsymbol{W}^{*}\| \le \overline{W}$ into (38), we have:

$$\begin{aligned}\|\boldsymbol{F}\| &\le \|\boldsymbol{W}^{*}\|\|\boldsymbol{\Phi}(\boldsymbol{Z})\| + \|\boldsymbol{\varepsilon}(\boldsymbol{Z})\| \\ &\le B\Phi,\end{aligned} \tag{39}$$

where $B = \max\{\overline{W}, \bar{\varepsilon}\}$ is an unknown constant and $\Phi = \|\boldsymbol{\Phi}(\boldsymbol{Z})\| + 1$ is a known function. Then, the neural integral sliding mode controller is developed as:

$$\boldsymbol{u} = -k_1\boldsymbol{s} - k_2\mathrm{sig}^{q}(\boldsymbol{s}) - \frac{\hat{B}_s\Phi^2\boldsymbol{s}}{2\eta^2}, \tag{40}$$

where $k_1 > 0, k_2 > 0, 0 < q < 1, \eta > 0$, $\hat{B}_s$ is the estimation of B_s; and $B_s = B^2$. Additionally, the parametric adaptive learning law is designed as:

$$\dot{\hat{B}}_s = -l_1\hat{B}_s + l_2\frac{\Phi^2\|\boldsymbol{s}\|^2}{2\eta^2}, \tag{41}$$

where $l_1 > 0$ and $l_2 > 0$.

Remark 2. *For the conventional neural and fuzzy approximations [45,46], the number of the adaptive parameters that were required to be learned online was* $3N$*. Alternatively, the mechanism of indirect neural approximation was introduced through inequality relaxation. Benefiting from this design, only a single learning parameter was required to be adjusted online, and the computation burden of the proposed controller was extremely reduced. The indirect neural approximation utilized in this article is more suitable for practical engineering, especially when considering that the onboard computer has a limited calculation capability.*

Remark 3. *In this article, the RBFNN was embedded into the integral sliding mode controller to compensate the lumped uncertainty and replace the robust switching term. It should be pointed out that the RBFNN utilized here can also be replaced by some other efficient approximation tools, such as a Chebyshev NN, wavelet NN, recurrent NN, cerebellar model articulation controller, extreme learning machine, or fuzzy logic system.*

Theorem 2. *Suppose the spacecraft system described as (2) and (3). When the neural integral sliding mode controller (40) and the parametric adaptive learning law (41) are employed, the*

resulting closed-loop system is practically finite-time stable, and the attitude and angular velocity tracking errors $\boldsymbol{\sigma}_e$ and $\boldsymbol{\omega}_e$ can regulate to the minor residual sets around zero in a finite time.

Proof. The proof of Theorem 2 involves two steps. In Step 1, we will prove that when the proposed controller $\boldsymbol{u}$ is employed, the integral sliding mode surface $\boldsymbol{s}$ can regulate to the minor residual set around zero in finite time. In Step 2, we will prove that when the integral sliding mode surface $\boldsymbol{s}$ arrives at zero, the attitude and angular velocity tracking errors $\boldsymbol{\sigma}_e$ and $\boldsymbol{\omega}_e$ can regulate to zero in finite time.

Step 1: Arriving phase. Introduce the following Lyapunov candidate function:

$$V_1 = \frac{1}{2}\boldsymbol{s}^{\mathrm{T}}\boldsymbol{J}\boldsymbol{s} + \frac{1}{2l_2\gamma_{\min}}\widetilde{B}_s^2, \tag{42}$$

where $\gamma_{\min} = \min\{\gamma_1, \gamma_2, \gamma_3\}$ and $\widetilde{B}_s = B_s - \gamma_{\min}\hat{B}_s$ denotes the estimation error of B_s. The time differentiation of V_1 can be evaluated as:

$$\begin{aligned} \dot{V}_1 &= \boldsymbol{s}^{\mathrm{T}}\boldsymbol{J}\dot{\boldsymbol{s}} - \tfrac{1}{l_2}\widetilde{B}_s\dot{\hat{B}}_s \\ &= \boldsymbol{s}^{\mathrm{T}}(\boldsymbol{\Gamma}\boldsymbol{u} + \boldsymbol{F}) - \tfrac{1}{l_2}\widetilde{B}_s\dot{\hat{B}}_s. \end{aligned} \tag{43}$$

Substituting the neural integral sliding mode controller (40) and the parametric adaptive learning law (41) into (43), we have:

$$\begin{aligned} \dot{V}_1 &= \boldsymbol{s}^{\mathrm{T}}\Big(\boldsymbol{\Gamma}\Big(-k_1\boldsymbol{s} - k_2\mathrm{sig}^q(\boldsymbol{s}) - \tfrac{\hat{B}_s\Phi^2\boldsymbol{s}}{2\eta^2}\Big) + \boldsymbol{F}\Big) - \widetilde{B}_s\Big(-\tfrac{l_1}{l_2}\hat{B}_s + \tfrac{\Phi^2\|\boldsymbol{s}\|^2}{2\eta^2}\Big) \\ &= -k_1\gamma_{\min}\|\boldsymbol{s}\|^2 - k_2\gamma_{\min}\|\boldsymbol{s}\|^{q+1} - \tfrac{B_s\Phi^2\|\boldsymbol{s}\|^2}{2\eta^2} + \boldsymbol{s}^{\mathrm{T}}\boldsymbol{F} + \tfrac{l_1}{l_2}\widetilde{B}_s\hat{B}_s. \end{aligned} \tag{44}$$

The following inequalities can be easily derived:

$$\boldsymbol{s}^{\mathrm{T}}\boldsymbol{F} \le \frac{B^2\Phi^2\|\boldsymbol{s}\|^2}{2\eta^2} + \frac{\eta^2}{2} = \frac{B_s\Phi^2\|\boldsymbol{s}\|^2}{2\eta^2} + \frac{\eta^2}{2}, \tag{45}$$

$$\frac{l_1}{l_2}\widetilde{B}_s\hat{B}_s = \frac{l_1}{l_2\gamma_{\min}}\widetilde{B}_s\Big(B_s - \widetilde{B}_s\Big) \le \frac{l_1}{2l_2\gamma_{\min}}\Big(B_s^2 - \widetilde{B}_s^2\Big). \tag{46}$$

Substituting (45) and (46) into (44), we have:

$$\begin{aligned} \dot{V}_1 &\le -k_1\gamma_{\min}\|\boldsymbol{s}\|^2 - k_2\gamma_{\min}\|\boldsymbol{s}\|^{q+1} - \tfrac{l_1}{2l_2\gamma_{\min}}\widetilde{B}_s^2 + \tfrac{l_1}{2l_2\gamma_{\min}}B_s^2 + \tfrac{\eta^2}{2} \\ &\le -k_1\gamma_{\min}\|\boldsymbol{s}\|^2 - \tfrac{l_1}{2l_2\gamma_{\min}}\widetilde{B}_s^2 + \tfrac{l_1}{2l_2\gamma_{\min}}B_s^2 + \tfrac{\eta^2}{2} \\ &\le -\beta V_1 + \psi, \end{aligned} \tag{47}$$

where $\beta = \min\Big\{\frac{2k_1\gamma_{\min}}{\lambda_{\max}(\boldsymbol{J})}, l_1\Big\}$ and $\psi = \frac{l_1}{2l_2\gamma_{\min}}B_s^2 + \frac{\eta^2}{2}$. Solving (46), we further have:

$$V_1 \le \Big(V_1(0) - \frac{\psi}{\beta}\Big)\mathrm{e}^{-\beta t} + \frac{\psi}{\beta}. \tag{48}$$

Combined with the definition of V_1, it follows that $\widetilde{B}_s$ is bounded. There exists an unknown positive constant $\overline{B}_s$ such that:

$$\Big|\widetilde{B}_s\Big| < \overline{B}_s. \tag{49}$$

Next, introduce another Lyapunov candidate function:

$$V_2 = \frac{1}{2}\boldsymbol{s}^{\mathrm{T}}\boldsymbol{J}\boldsymbol{s}. \tag{50}$$

Likewise, the time differentiation of V_2 can be evaluated as:

$$\begin{aligned}\dot{V}_2 &= \boldsymbol{s}^{\mathrm{T}}\boldsymbol{J}\dot{\boldsymbol{s}} \\ &= \boldsymbol{s}^{\mathrm{T}}\left(\boldsymbol{I}\left(-k_1\boldsymbol{s} - k_2\mathrm{sig}^q(\boldsymbol{s}) - \frac{\hat{B}_s\Phi^2\boldsymbol{s}}{2\eta^2}\right) + \boldsymbol{F}\right) \\ &\leq -k_1\gamma_{\min}\|\boldsymbol{s}\|^2 - k_2\gamma_{\min}\|\boldsymbol{s}\|^{q+1} + \frac{\widetilde{B}_s\Phi^2\|\boldsymbol{s}\|^2}{2\eta^2} + \frac{\eta^2}{2}.\end{aligned} \tag{51}$$

Substituting (49) into (51), we have:

$$\begin{aligned}\dot{V}_2 &\leq -k_1\gamma_{\min}\|\boldsymbol{s}\|^2 - k_2\gamma_{\min}\|\boldsymbol{s}\|^{q+1} + \frac{\overline{B}_s\Phi^2\|\boldsymbol{s}\|^2}{2\eta^2} + \frac{\eta^2}{2}. \\ &\leq -\left(k_1\gamma_{\min} - \frac{\overline{B}_s\Phi^2}{2\eta^2}\right)\|\boldsymbol{s}\|^2 - k_2\gamma_{\min}\|\boldsymbol{s}\|^{q+1} + \frac{\eta^2}{2} \\ &= -\kappa_1 V_2 - \kappa_2 V_2^{\frac{q+1}{2}} + \vartheta,\end{aligned} \tag{52}$$

where $\kappa_1 = \frac{2k_1\gamma_{\min} - \frac{\overline{B}_s\Phi^2}{\eta^2}}{\lambda_{\max}(\boldsymbol{J})}$, $\kappa_2 = \frac{2k_2\gamma_{\min}}{\lambda_{\max}^{\frac{q+1}{2}}(\boldsymbol{J})}$, and $\vartheta = \frac{\eta^2}{2}$. To ensure $\kappa_1 > 0$, the design parameter k_1 should be selected to satisfy the following condition:

$$k_1 > \frac{\overline{B}_s\Phi^2}{2\eta^2\gamma_{\min}}. \tag{53}$$

Then, using Lemma 2, the resulting closed-loop system becomes practically finite-time stable, and V_2 can regulate to the following minor residual set around zero in finite time:

$$C = \left\{ V_2 \middle| V_2 \leq \frac{\vartheta}{(1-\varsigma)\kappa_1} \right\}, \tag{54}$$

where $0 < \varsigma < 1$. Combined with the definition of V_2, it follows that the integral sliding mode surface $\boldsymbol{s}$ can regulate to the minor residual set around zero in a finite time. Moreover, the finite settling time of the arriving phase can be estimated as:

$$T_{arriving} \leq \frac{2}{\varsigma\kappa_1(1-q)} \ln \frac{\varsigma\kappa_1 V_2^{\frac{1-q}{2}}(0) + \kappa_2}{\kappa_2}. \tag{55}$$

Step 2: Sliding phase. According to Theorem 1, when the integral sliding mode surface $\boldsymbol{s}$ arrives at zero, the attitude and angular velocity tracking errors $\boldsymbol{\sigma}_e$ and $\boldsymbol{\omega}_e$ can regulate to zero in finite time.

From the results of Steps 1 and 2, we can obtain that the resulting closed-loop system is practically finite-time stable, and the attitude and angular velocity tracking errors $\boldsymbol{\sigma}_e$ and $\boldsymbol{\omega}_e$ can regulate to the minor residual sets around zero in a finite time. Moreover, the total finite settling time can be estimated as:

$$T_{total} = T_{arriving} + T_{sliding} \leq \frac{2}{\varsigma\kappa_1(1-q)} \ln \frac{\varsigma\kappa_1 V_2^{\frac{1-q}{2}}(0) + \kappa_2}{\kappa_2} + \frac{2pL^{\frac{p-1}{2p}}(0)}{\alpha(p-1)}. \tag{56}$$

In addition, it can be obtained from (54) that the minor residual sets around zero are adjustable. If the design parameters k_1 and k_2 are selected as large as desired, the minor residual sets can be made sufficiently minor. The proof is thus finished. □

Remark 4. *A unified parameter selection approach for the proposed controller was carried out. First, we determined p, h_1, and h_2 in the integral sliding mode surface (17); p should be selected as a ratio of two positive odd integers satisfying $1 < p < 2$, and h_1 and h_2 should be selected to satisfy the conditions (18) and (19). In general, a small h_1 and large h_2 can increase the convergence rate. However, the control torques become large at the same time. Then, we determined q, k_1, and k_2 in the neural integral sliding mode controller (40); q should be selected to satisfy $0 < q < 1$.*

In general, a large k_1 and k_2 can accelerate the convergence. However, they may in turn lead to the relatively large control torques. Finally, we determined η, l_1, and l_2. In general, a small l_1 and large l_2 can speed up the convergence. However, they may also result in a relatively poor transient response performance. Therefore, to achieve an excellent tracking performance, the parameters of the proposed controller must be appropriately selected through trial and error.

Remark 5. *For convenience of the readers to reach a better understanding, the structure of the proposed neural integral sliding mode control strategy is depicted in Figure 1.*

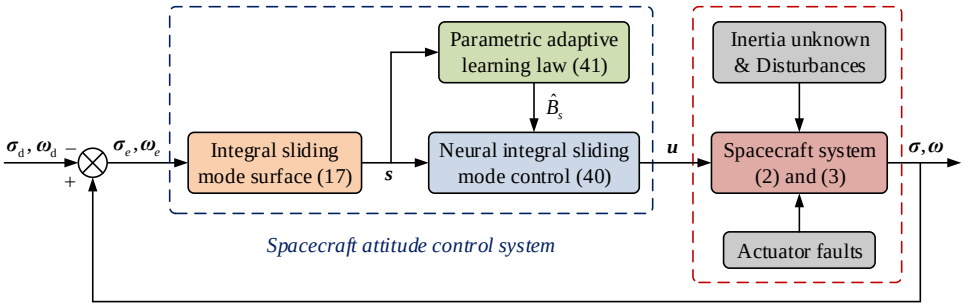

Figure 1. Structure of the proposed neural integral sliding mode control strategy.

4. Simulations and Comparisons

In this section, simulations and comparisons are conducted to demonstrate the proposed neural integral sliding mode control strategy. The inertia matrix of the spacecraft is presented as [52]:

$$\boldsymbol{J} = \begin{bmatrix} 20 & 1.2 & 0.9 \\ 1.2 & 17 & 1.4 \\ 0.9 & 1.4 & 15 \end{bmatrix} \text{kg} \cdot \text{m}^2. \tag{57}$$

The inertia matrix was fully unknown for the control design. The disturbances were given as $\boldsymbol{d} = [0.04\sin(0.4t), 0.02\sin(0.8t), 0.03\sin(0.6t)]^{\mathrm{T}}$ Nm. The actuation effectiveness matrix was chosen as:

$$\boldsymbol{\Gamma} = \text{diag}\{0.8 + 0.1\sin(1.8t), 0.7 + 0.1\cos(2.1t), 0.8 + 0.1\sin(2.4t)\}. \tag{58}$$

Moreover, the initial attitude and angular velocity of the spacecraft were provided as $\sigma_0 = [0.3, 0.2, -0.2]^{\mathrm{T}}$ and $\boldsymbol{\omega}_0 = [0.01, 0.02, -0.02]^{\mathrm{T}}$rad/s, respectively. The desired attitude of the spacecraft was set as $\sigma_{\mathrm{d}} = 0.04[\sin(0.21t), \sin(0.24t), \sin(0.18t)]^{\mathrm{T}}$.

In addition to the proposed neural integral sliding mode controller (40), another two finite-time model-free controllers were also employed for comparisons. They were the finite-time controller designed based on the homogeneous method in [18] and the finite-time controller developed by using the technique of adding a power integrator in [21]. Specifically, the finite-time controller in [18] was formulated as:

$$\boldsymbol{u} = -k_1 \boldsymbol{G}^{-1}(\sigma_e)\text{sig}^{\alpha_1}(\sigma_e) - k_2 \text{sig}^{\alpha_2}(\boldsymbol{\omega}_e), \tag{59}$$

where $k_1 > 0$, $k_2 > 0$, $0 < \alpha_1 < 1$, and $\alpha_2 = 2\alpha_1/(1 + \alpha_1)$. Moreover, the finite-time controller in [21] was carried out as:

$$\boldsymbol{u} = -k_2 \left(\frac{1 + \sigma_e^{\mathrm{T}} \sigma_e}{4} \right) \left(\boldsymbol{\omega}_e^p + k_1^p \sigma_e \right)^{\frac{2}{p} - 1}, \tag{60}$$

where $k_1 > 0$, $k_2 > 0$, and $1 < p = p_1/p_2 < 2$, and p_1 and p_2 are positive odd integers.

The parameters of the proposed neural-enhanced integral TSM controller (39) were selected as $h_1 = 1.2$, $h_2 = 3$, $p = 101/99$, $k_1 = 20$, $k_2 = 20$, $q = 4/5$, $l_1 = 1$, $l_2 = 1$, and $\eta = 0.1$. Seven nodes were set for the hidden layer of the RBFNN. The parameters

of the RBFNN were selected as $\boldsymbol{c}_i = [-3,-2,-1,0,1,2,3]^{\mathrm{T}}$ and $w_i = 6$. Moreover, the parameters of the compared finite-time controller (59) were selected as $k_1 = 5$, $k_2 = 12$, and $\alpha_1 = 4/5$. The parameters of the compared finite-time controller (60) were selected as $k_1 = 1.2$, $k_2 = 30$, and $p = 11/9$.

Figures 2 and 3 show the profiles of the attitude and angular velocity tracking, respectively. It can be clearly seen that the spacecraft could accomplish the attitude tracking task successfully under the proposed and compared controllers. The profiles of the attitude and angular velocity tracking errors are presented in Figures 4 and 5, respectively. The proposed controller could achieve the excellent tracking performance even when subject to lumped uncertainty. By contrast, the tracking performances of the two compared controllers were relatively poor due to the existence of actuator faults, unknown inertia, and disturbances. Quantitatively, the steady-state attitude and angular velocity tracking errors under the proposed controller were within the ranges of $\left[-5\times10^{-4}, 5\times10^{-4}\right]$ and $\left[-1\times10^{-3}, 1\times10^{-3}\right]$ rad/s, which could meet the requirements of most practical space missions. However, the steady-state attitude and angular velocity tracking errors under the two compared controllers were within the ranges of $\left[-5\times10^{-3}, 5\times10^{-3}\right]$ and $\left[-6\times10^{-3}, 6\times10^{-3}\right]$ rad/s. Therefore, the proposed controller could realize a higher steady-state attitude and angular velocity tracking accuracy than the two compared controllers. This mainly benefited from the superior uncertainty attenuation capability of the proposed controller by employing the NN for feedforward compensation. The profile of the control torques is shown in Figure 6. It is not difficult to find that the control torques of the proposed and compared controllers were always within the reasonable range during the entire attitude tracking process. Figure 7 gives the profile of the adaptive parameter. The convergence time of the adaptive parameter was about 14.5 s, which was nearly the same as the convergence time of the attitude and angular velocity tracking. Moreover, it should be emphasized that only one adaptive learning parameter was required to be adjusted online for the indirect neural approximation, and the onboard calculation burden of the proposed controller was extremely reduced. This distinctive feature of the proposed controller gives it potential for practical applications.

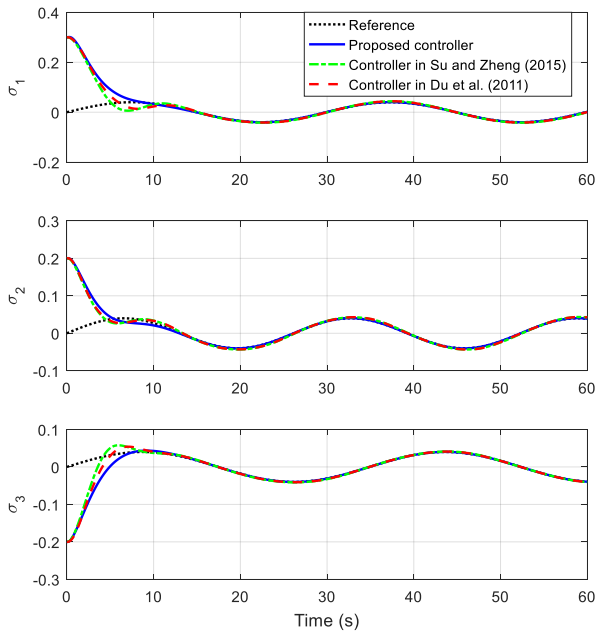

Figure 2. Profile of the attitude tracking σ [18,21].

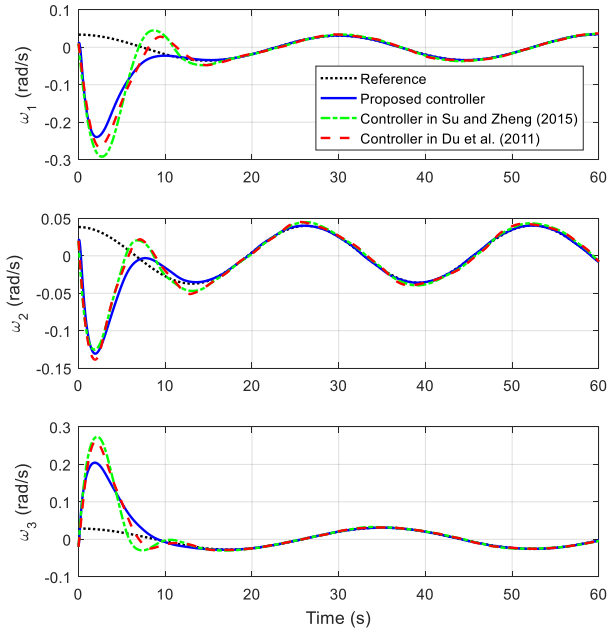

Figure 3. Profile of the angular velocity tracking ω [18,21].

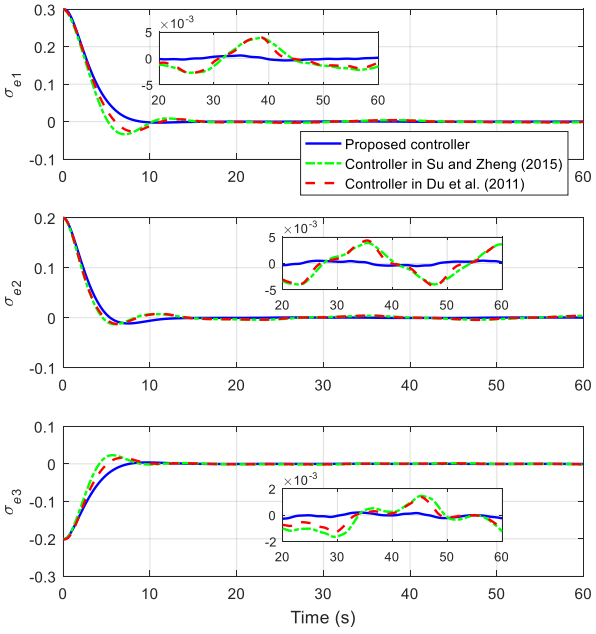

Figure 4. Profile of the attitude tracking errors σ_e [18,21].

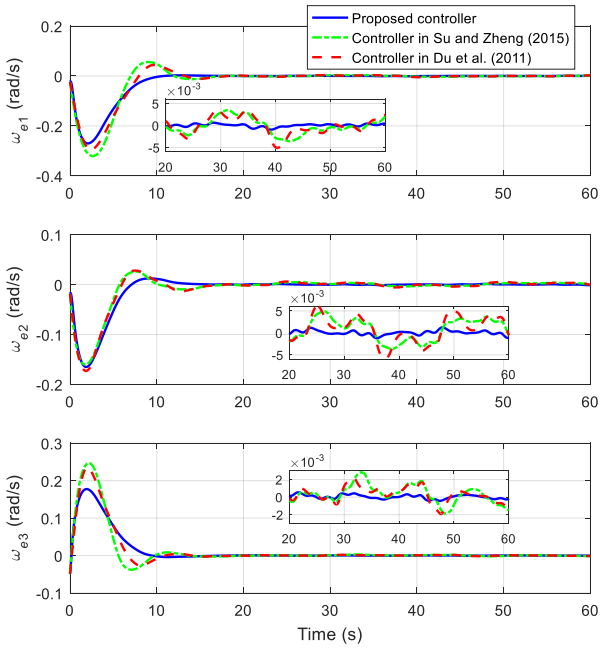

Figure 5. Profile of the angular velocity tracking errors $\boldsymbol{\omega}_e$ [18,21].

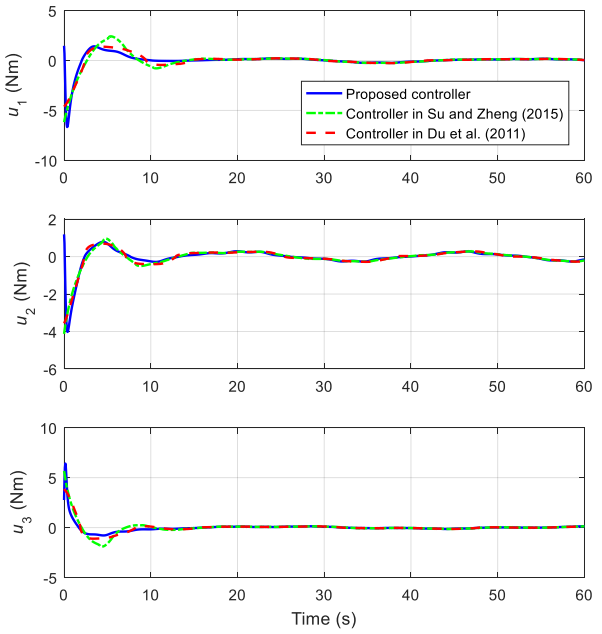

Figure 6. Profile of the control torques $\boldsymbol{u}$ [18,21].

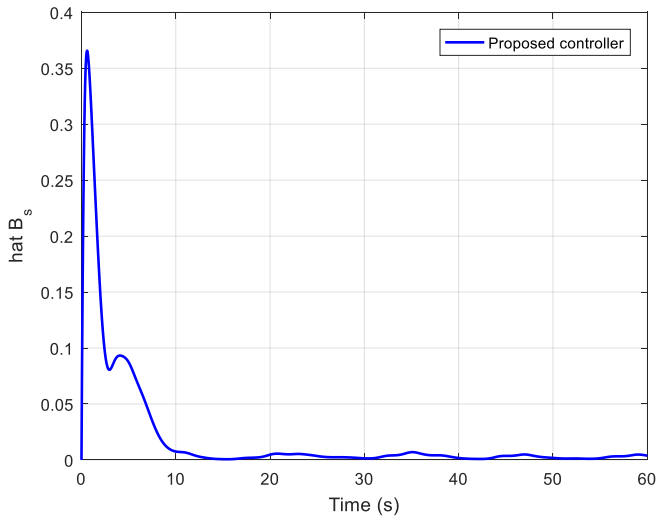

Figure 7. Profile of the adaptive parameter $\hat{B}$.

Furthermore, Figures 8 and 9 provide the norms of the attitude and angular velocity tracking errors, respectively, under the proposed and compared controllers. The energy consumptions of the three controllers are depicted in Figure 10, where the energy consumption index is defined as $E_u = \frac{1}{2}\int_0^t \|\boldsymbol{u}(\tau)\|\mathrm{d}\tau$. As shown in Figures 8–10, it is obvious that the proposed controller could achieve a more excellent tracking performance than the two compared controllers, associated with faster convergence rate, higher tracking accuracy, and less energy consumption. As discussed in the Introduction, the finite-time controller designed based on the homogeneous method in [18] and the finite-time controller developed by using the technique of adding a power integrator in [21] had difficulty handling the unknown inertia, disturbances, and actuator faults. Alternatively, the proposed controller was designed as a combination of integral sliding mode control and indirect neural approximation. Benefiting from the indirect neural compensation, the proposed controller was not only strongly robust against unknown inertia and disturbances, but also highly insensitive to actuator faults.

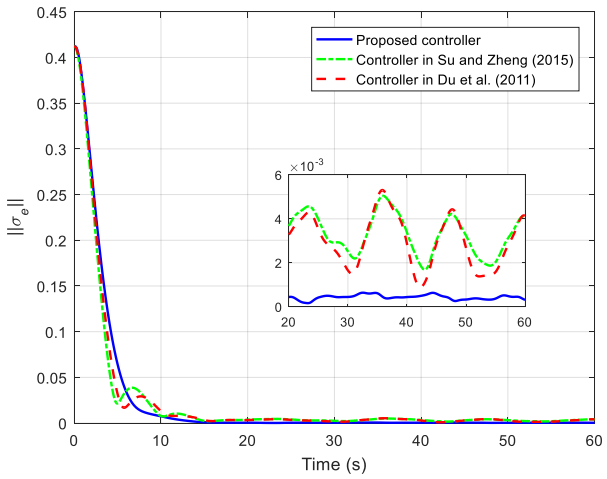

Figure 8. Norm of the attitude tracking errors $\|\sigma_e\|$ [18,21].

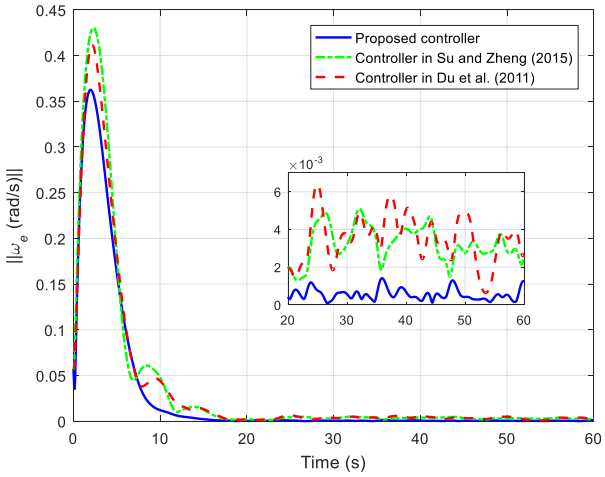

Figure 9. Norm of the angular velocity tracking errors $\|\omega_e\|$ [18,21].

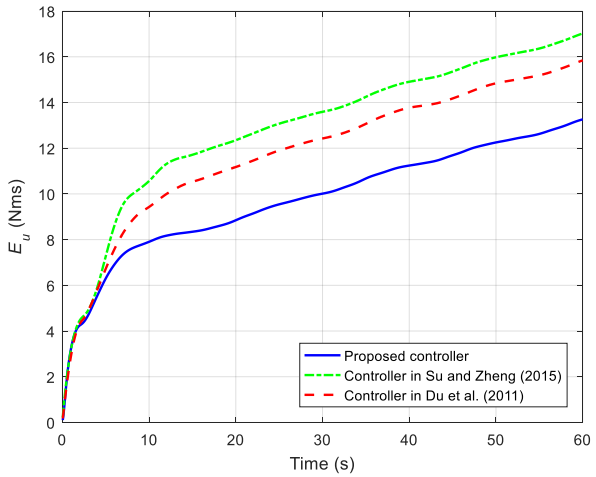

Figure 10. Profile of the energy consumption index E_u [18,21].

5. Conclusions

This article aimed to present a neural integral sliding mode control strategy for the finite-time attitude tracking of uncertain spacecraft in the presence of actuator faults. Based on the novel integral sliding mode surface, the proposed controller was developed through integration with the indirect neural approximation to compensate the lumped uncertainty. The practical finite-time stability of the resulting closed-loop system was achieved through theoretical analysis. The proposed controller could ensure that the attitude and angular velocity tracking errors were stabilized to the minor residual sets around zero in a finite time. Moreover, the minor residual sets around zero were adjustable, and could be made as small as possible by properly selecting the design parameters. It should be pointed out that both the singularity problem and the chattering phenomenon commonly existing in the conventional terminal sliding mode control were well addressed through the proposed control design. Finally, the simulation results indicated the excellent tracking performance and good uncertainty rejection capability of the proposed control strategy. Future investigation of this work will be deployed by improving the proposed control strategy with the fixed-time convergence property.

Author Contributions: Conceptualization, Q.Y., H.J., S.B., S.F.M. and N.D.A.; methodology, Q.Y., H.J., S.B., S.F.M. and N.D.A.; software, Q.Y., H.J., S.B., S.F.M. and N.D.A.; validation, Q.Y., H.J., S.B., S.F.M. and N.D.A.; investigation, Q.Y., H.J., S.B., S.F.M. and N.D.A.; writing—original draft preparation, Q.Y., H.J., S.B., S.F.M. and N.D.A.; writing—review and editing, Q.Y., H.J., S.B., S.F.M. and N.D.A.;

supervision, Q.Y., H.J., S.B., S.F.M. and N.D.A. All authors have read and agreed to the published version of the manuscript.

Funding: This research work was funded by Institutional Fund Projects under Grant no. (IFPDP-231-22). Therefore, the authors gratefully acknowledge technical and financial support from the Ministry of Education and King Abdulaziz University (KAU), Jeddah, Saudi Arabia.

Informed Consent Statement: Not applicable.

Acknowledgments: This research work was funded by Institutional Fund Projects under Grant no. (IFPDP-231-22). Therefore, the authors gratefully acknowledge technical and financial support from the Ministry of Education and King Abdulaziz University (KAU), Jeddah, Saudi Arabia.

Conflicts of Interest: The authors declare no conflict of interest.

References

1. Wen, J.Y.; Kreutz-Delgado, K. The attitude control problem. *IEEE Trans. Autom. Control* **1991**, *36*, 1148–1162. [CrossRef]
2. Tsiotras, P. Further passivity results for the attitude control problem. *IEEE Trans. Autom. Control* **1998**, *43*, 1597–1600. [CrossRef]
3. Su, Y.; Zheng, C. Globally asymptotic stabilization of spacecraft with simple saturated proportional-derivative control. *J. Guid. Control Dyn.* **2011**, *34*, 1932–1936. [CrossRef]
4. Su, Y.; Zheng, C. Velocity-free saturated PD control for asymptotic stabilization of spacecraft. *Aerosp. Sci. Technol.* **2014**, *39*, 6–12. [CrossRef]
5. Lo, S.-C.; Chen, Y.-P. Smooth sliding-mode control for spacecraft attitude tracking maneuvers. *J. Guid. Control Dyn.* **1995**, *18*, 1345–1349. [CrossRef]
6. Yeh, F.-K. Sliding-mode adaptive attitude controller design for spacecraft with thrusters. *IET Control. Theory Appl.* **2010**, *4*, 1254–1264. [CrossRef]
7. Zhu, Z.; Xia, Y.; Fu, M. Adaptive sliding mode control for attitude stabilization with actuator saturation. *IEEE Trans. Ind. Electron.* **2011**, *58*, 4898–4907. [CrossRef]
8. Lu, K.; Xia, Y.; Zhu, Z.; Basin, M.V. Sliding mode attitude tracking of rigid spacecraft with disturbances. *J. Frankl. Inst.* **2012**, *349*, 413–440. [CrossRef]
9. Kristiansen, R.; Nicklasson, P.J.; Gravdahl, J.T. Satellite attitude control by quaternion-based backstepping. *IEEE Trans. Control Syst. Technol.* **2009**, *17*, 227–232. [CrossRef]
10. Ali, I.; Radice, G.; Kim, J. Backstepping control design with actuator torque bound for spacecraft attitude maneuver. *J. Guid. Control Dyn.* **2010**, *33*, 254–259. [CrossRef]
11. Wu, B.; Wang, D.; Poh, E.K. High precision satellite attitude tracking control via iterative learning control. *J. Guid. Control Dyn.* **2015**, *38*, 528–534. [CrossRef]
12. Yao, Q. Robust adaptive iterative learning control for high precision attitude tracking of spacecraft. *J. Aerosp. Eng.* **2021**, *34*, 04020108. [CrossRef]
13. Leeghim, H.; Choi, Y.; Bang, H. Adaptive attitude control of spacecraft using neural networks. *Acta Astronaut* **2009**, *64*, 778–786. [CrossRef]
14. Zou, A.-M.; Kumar, K.D. Adaptive fuzzy fault-tolerant attitude control of spacecraft. *Control Eng. Pract.* **2011**, *19*, 10–21. [CrossRef]
15. Li, M.; Hou, M.; Yin, C. Adaptive attitude stabilization control design for spacecraft under physical limitations. *J. Guid. Control Dyn.* **2016**, *39*, 2176–2180. [CrossRef]
16. Huo, B.; Xia, Y.; Yin, L.; Fu, M. Fuzzy adaptive fault-tolerant output feedback attitude-tracking control of rigid spacecraft. *IEEE Trans. Syst. Man. Cybern. Syst.* **2017**, *47*, 1898–1908. [CrossRef]
17. Du, H.; Li, S. Finite-time attitude stabilization for a spacecraft using homogeneous method. *J. Guid. Control Dyn.* **2012**, *35*, 740–748.
18. Su, Y.; Zheng, C. Simple nonlinear proportional-derivative control for global finite-time stabilization of spacecraft. *J. Guid. Control Dyn.* **2015**, *38*, 173–178.
19. Gui, H.; Jin, L.; Xu, S. Simple finite-time attitude stabilization laws for rigid spacecraft with bounded inputs. *Aerosp. Sci. Technol.* **2015**, *42*, 176–186. [CrossRef]
20. Zou, A.-M.; de Ruiter, A.H.J.; Kumar, K.D. Finite-time output feedback attitude control for rigid spacecraft under control input saturation. *J. Frankl. Inst.* **2016**, *353*, 4442–4470.
21. Du, H.; Li, S.; Qian, C. Finite-time attitude tracking control of spacecraft with application to attitude synchronization. *IEEE Trans. Autom. Control* **2011**, *56*, 2711–2717. [CrossRef]
22. Jiang, B.; Li, C.; Ma, G. Finite-time output feedback attitude control for spacecraft using "Adding a power integrator" technique. *Aerosp. Sci. Technol.* **2017**, *66*, 342–354. [CrossRef]
23. Zhao, L.; Yu, J.; Yu, H. Adaptive finite-time attitude tracking control for spacecraft with disturbances. *IEEE Trans. Aerosp. Electron. Syst.* **2018**, *54*, 1297–1305. [CrossRef]
24. Yao, Q. Robust finite-time control design for attitude stabilization of spacecraft under measurement uncertainties. *Adv. Space Res.* **2021**, *68*, 3159–3175. [CrossRef]

25. Jin, E.; Sun, Z. Robust controllers design with finite time convergence for rigid spacecraft attitude tracking control. *Aerosp. Sci. Technol.* **2018**, *12*, 324–330. [CrossRef]
26. Li, S.; Wang, Z.; Fei, S. Comments on the paper: Robust controllers design with finite time convergence for rigid spacecraft attitude tracking control. *Aerosp. Sci. Technol.* **2011**, *15*, 193–195. [CrossRef]
27. Zhu, Z.; Xia, Y.; Fu, M. Attitude stabilization of rigid spacecraft with finite-time convergence. *Int. J. Robust Nonlinear Control* **2011**, *21*, 686–702. [CrossRef]
28. Lu, K.; Xia, Y. Adaptive attitude tracking control for rigid spacecraft with finite-time convergence. *Automatica* **2013**, *49*, 3591–3599. [CrossRef]
29. Song, Z.; Li, H.; Sun, K. Finite-time control for nonlinear spacecraft attitude based on terminal sliding mode technique. *ISA Trans.* **2014**, *53*, 117–124. [CrossRef]
30. Pukdeboon, C.; Siricharuanun, P. Nonsingular terminal sliding mode based finite-time control for spacecraft attitude tracking. *Int. J. Control Autom. Syst.* **2014**, *12*, 530–540. [CrossRef]
31. Han, Z.; Zhang, K.; Yang, T.; Zhang, M. Spacecraft fault-tolerant control using adaptive non-singular fast terminal sliding mode. *IET Control Theory Appl.* **2016**, *10*, 1991–1999. [CrossRef]
32. Shao, S.; Zong, Q.; Tian, B.; Wang, F. Finite-time sliding mode attitude control for rigid spacecraft without angular velocity measurement. *J. Frankl. Inst.* **2017**, *354*, 4656–4674. [CrossRef]
33. Song, Z.; Duan, C.; Su, H.; Hu, J. Full-order sliding mode control for finite-time attitude tracking of rigid spacecraft. *IET Control Theory Appl.* **2018**, *12*, 1086–1094. [CrossRef]
34. Guo, Y.; Huang, B.; Song, S.; Li, A.; Wang, C. Robust saturated finite-time attitude control for spacecraft using integral sliding mode. *J. Guid. Control Dyn.* **2019**, *42*, 440–446. [CrossRef]
35. Jahanshahi, H.; Yousefpour, A.; Munoz-Pacheco, J.M.; Moroz, I.; Wei, Z.; Castillo, O. A new multi-stable fractional-order four-dimensional system with self-excited and hidden chaotic attractors: Dynamic analysis and adaptive synchronization using a novel fuzzy adaptive sliding mode control method. *Appl. Soft Comput.* **2020**, *87*, 105943. [CrossRef]
36. Wang, S.; Bekiros, S.; Yousefpour, A.; He, S.; Castillo, O.; Jahanshahi, H. Synchronization of fractional time-delayed financial system using a novel type-2 fuzzy active control method. *Chaos Solitons Fractals* **2020**, *136*, 109768. [CrossRef]
37. Xiong, P.-Y.; Jahanshahi, H.; Alcaraz, R.; Chu, Y.-M.; Gómez-Aguilar, J.F.; Alsaadi, F.E. Spectral entropy analysis and synchronization of a multi-stable fractional-order chaotic system using a novel neural network-based chattering-free sliding mode technique. *Chaos Solitons Fractals* **2021**, *144*, 110576. [CrossRef]
38. Li, J.-F.; Jahanshahi, H.; Kacar, S.; Chu, Y.-M.; Gómez-Aguilar, J.F.; Alotaibi, N.D.; Alharbi, K.H. On the variable-order fractional memristor oscillator: Data security applications and synchronization using a type-2 fuzzy disturbance observer-based robust control. *Chaos Solitons Fractals* **2021**, *145*, 110681. [CrossRef]
39. Bekiros, S.; Jahanshahi, H.; Bezzina, F.; Aly, A.A. A novel fuzzy mixed H_2/H_∞ optimal controller for hyperchaotic financial systems. *Chaos Solitons Fractals* **2021**, *146*, 110878. [CrossRef]
40. Wang, Y.-L.; Jahanshahi, H.; Bekiros, S.; Bezzina, F.; Chu, Y.-M.; Aly, A.A. Deep recurrent neural networks with finite-time terminal sliding mode control for a chaotic fractional-order financial system with market confidence. *Chaos Solitons Fractals* **2021**, *146*, 110881. [CrossRef]
41. Yao, Q. Adaptive fuzzy neural network control for a space manipulator in the presence of output constraints and input nonlinearities. *Adv. Space Res.* **2021**, *67*, 1830–1843. [CrossRef]
42. Yao, Q. Adaptive trajectory tracking control of a free-flying space manipulator with guaranteed prescribed performance and actuator saturation. *Acta Astronaut* **2021**, *185*, 283–298. [CrossRef]
43. Yao, Q. Neural adaptive learning synchronization of second-order uncertain chaotic systems with prescribed performance guarantees. *Chaos Solitons Fractals* **2021**, *152*, 111434. [CrossRef]
44. Alsaade, F.W.; Yao, Q.; Al-zahrani, M.S.; Alzahrani, A.S.; Jahanshahi, H. Indirect-neural approximation-based fault-tolerant integrated attitude and position control of spacecraft proximity operations. *Sensors* **2022**, *22*, 1726. [CrossRef]
45. Zou, A.-M.; Kumar, K.D.; Hou, Z.-G.; Liu, X. Finite-time attitude tracking control for spacecraft using terminal sliding mode and Chebyshev neural network. *IEEE Trans. Syst. Man. Cybern Part B Cybern* **2011**, *41*, 950–963.
46. Huo, B.; Xia, Y.; Lu, K.; Fu, M. Adaptive fuzzy finite-time fault-tolerant attitude control of rigid spacecraft. *J. Frankl. Inst.* **2015**, *352*, 4225–4246. [CrossRef]
47. Hughes, P.C. *Spacecraft Attitude Dynamics*; John Wiley and Sons: New York, NY, USA, 1986.
48. Bhat, S.P.; Bernstein, D.S. Finite-time stability of continuous autonomous systems. *SIAM J. Control Optim.* **2000**, *38*, 751–766. [CrossRef]
49. Yao, Q. Adaptive finite-time sliding mode control design for finite-time fault-tolerant trajectory tracking of marine vehicles with input saturation. *J. Frankl. Inst.* **2020**, *357*, 13593–13619. [CrossRef]
50. Sanner, R.M.; Slotine, J.-J.E. Gaussian networks for direct adaptive control. *IEEE Trans. Neural. Netw.* **1992**, *3*, 837–863. [CrossRef]
51. Hardy, G.H.; Littlewood, J.E.; Pólya, G. *Inequalities*; Cambridge University Press: Cambridge, MA, USA, 1952.
52. Ahmed, J.; Vincent, T.C.; Bernstein, D.S. Adaptive asymptotic tracking of spacecraft attitude motion with inertia matrix identification. *J. Guid. Control Dyn.* **1998**, *21*, 684–691. [CrossRef]